Multi-hit damage and perforation of plates inspired by the attacks of the mantis shrimp

P. De Falco [a,d], F. Ongaro [b,c], N.M. Pugno [c,d,*]

[a] *EUROCONTROL Innovation Hub (EIH), Bretigny-Sur-Orge, France*
[b] *Department of Weapon Systems and Ballistics, Royal Military Academy, 30 Avenue de la Renaissance, 1000 Brussels, Belgium*
[c] *Laboratory for Bio-Inspired, Bionic, Nano, Meta Materials & Mechanics, Department of Civil, Environmental and Mechanical Engineering, University of Trento, Trento, Italy*
[d] *Queen Mary University of London, School of Engineering and Material Science, London, E1 4NS, UK*

ABSTRACT

The crustacean *Odontodactylus scyllarus*, known as peacock mantis shrimp, employs its hammer-like appendages to attack and destroy the shells of prey with a sequence of two strikes. The first strong strike of about 480 N triggers a cavitation bubble in the seawater, which provokes a successive hit (about twice weaker than the first one and with a time delay of ≈0.5 ms) on the prey upon collapsing. Inspired by this double-impact strategy, this paper presents a set of parametric finite element simulations of single, double and triple mechanical hits, using elastic-plastic targets and rigid-body projectiles, to compute the damage energy of the target. Several sequences of combinations (strong, weak and equal impact energy), different diameters of the projectile, (3, 4, 6) mm, and various time delays between consecutive impacts, taken in the range 0.0–0.8 ms, are tested by keeping the total impact energy of the projectile fixed and equal to 2.27 J. Our results reveal that: (i) the single-impact strategy is the most damaging, (ii) among the double-impact cases the crustacean attack strategy has the most damaging effect, (iii) the triple-impact strategy shows more complex scenarios and different optimal solutions. Our results could be of interest for designing bio-inspired armours.

1. Introduction

Impact events often occur in biology and it would be difficult to quote without omissions the large number of situations in which biological systems are subjected to impact loading conditions.

Emblematic is the case of the deer fighting that represents not only a very famous example of biological impact (Currey et al., 2009) but also a fascinating example of high fracture toughness (Gupta et al., 2013; Hang et al., 2014). These animals, as reported in (Clutton-Brock, 1988), use their antler during the battles with other deer for defensive purposes or to gain dominance and access to female. Although most of the impact energy is absorbed by the neck muscles, antler bone contributes to locally dissipate energy and is designed to undergo high impact loading and large bending moments without fracture. A similar behavior is described in (Kitchener, 1987) in the case of antelopes, gazelles and goats that use their horns as impact-resistant weapons for defence and offence. Other impact loading situations involve Chimpanzees,

Capuchin monkeys in Brazil and Macaques in Southern Thailand, which employ stones to break nuts and hard-shelled fruits, and the sea otters that drive bivalve shells against their chest or emergent rocks at a velocity of approximately 1–2 m/s (Lazarus et al., 2020; Haslam et al., 2019). An analogous hammering strategy is adopted by the *Haematopus bachmani* (black oystercatcher) to separate the two valves of the oyster. This bird, as illustrated in (Butler and Kirbyson, 1979), uses its bill to firstly perforate the shell of the oyster and, finally, to sever the adductor muscles of the mollusc to prevent it from providing resistance. Other studies (Carlin and Gladstein, 1989; Gronenberg, 1995), focusing on the mechanisms of impact in biological structures, investigated how the smasher function of ant mandibles is involved in catching preys and in defence against other ants. According to the authors, ants use the mechanical energy stored in the muscles closer to the mandible not only to capture preys but also as an efficient propulsion to jump over competitor and escape.

The woodpecker's beak (Wang et al., 2013) and the galloping horse's

---

hoof (Lazarus et al., 2020) are two additional examples of biological systems subjected to repeated medium-velocity impacts, being the first hitting the target at approximately 7 m/s (Lazarus et al., 2020) and the second impacting the ground at about 8 m/s (Parsons et al., 2011). By referring the interested reader to the comprehensive reviews in (Lazarus et al., 2020; Meyers et al., 2008b; Chen et al., 2012) for an extended list of impact situations in biology, a final example that deserves our attention is the *Odontodactylus scyllarus* (subphylum: Crustacea, order: Stomatopoda, family: Gonodactylidae), one of the around 500 species of mantis shrimp that have been discovered. This crustacean, commonly called 'the mantis shrimp', is currently receiving prominent interest in the literature because of its very effective visual system (Cronin and Marshall, 1989; Cronin et al., 2001; Thoen et al., 2014), with 12-channel cooler vision, and, above all, because of its ability to deliver one of the fastest and powerful strikes in the animal kingdom, at accelerations over 10^5 m/s^2 and impact forces up to 1500 N (Tadayon et al., 2018; Behera and Le Ferrand, 2021). Such unusual performance is possible thanks to large raptorial hammer-like appendages that the mantis shrimp uses for different purposes, as to construct and excavate burrows, for territorial fights with conspecifics, to defend against predators and, finally, for hunting. Regarding the latter, according to the literature the mantis shrimp's strikes are so fast and powerful that can smash and perforate the shells of prey, like crabs, and snails which kill these animals instantaneously (Caldwell and Dingle, 1975, 1976; Dingle and Caldwell, 1969). In order to generate such extreme velocities, up to 23 m/s underwater, and accelerations of their strikes, mantis shrimps are tough to utilise a particular power amplification mechanism that, from a mechanical point of view, can be conceived as a system of elastic springs, latches and lever arms (Patek, 2019). Specifically, a specialised spring, i. e., a saddle-shaped element, initially stores the elastic energy coming from the contraction of extensor muscles while, as typical for spring-driven movements, a latch mechanisms, i.e., a set of mineralized sclerites activated by flexor muscles in the menus, prevents the raptorial appendage to move during the spring-loading phase and lock the system in the loaded configuration. Then, once the animal is ready to strike, the activity of the flexor and extensor muscles stops and the release of the mechanism occurs: the sclerites are unlocked and the elastic energy stored in the spring is released, allowing the appendage to rotate and hit the target. A consequence of the extreme speed of these strikes, combined with their location underwater, is the generation of cavitation bubbles at the site of the impact, between the mantis shrimp's appendages and the striking surface (Burrows and Hoyle, 1972).

Cavitation, that consists in the formation of vapour bubbles when a force acts upon a liquid, is a destructive phenomenon since the collapse of such bubbles leads to large-amplitude shock waves, associated with the release of energy in the form of heat, noise and luminescence (Brennen, 2013). Specifically, cavitation occurs at the interface between a solid structure and the flow when nuclei containing small amount of gas become unstable and grow due to a reduction of the ambient pressure. With reference to the mantis shrimp's attack, this condition is verified because of the separated flow generated by the fast rebound of the dactyl after hitting the prey. Also, for the mantis shrimp, the successive collapse of the cavitation bubbles is advantageous since it provokes a second strike force against the prey. As reported in (Patek and Caldwell, 2005), to which we refer the interested reader for a detailed description of the mantis shrimp's complex sequence of spring-actuated, latch-mediated movements, the second strike is generally twice wicker than the first one, due to the appendage physically striking the target. In particular, based on force measurements, acoustic analysis and high-speed imaging, the authors found that, in the case of the peacock mantis shrimp *Odontodactylus scyllarus*, the intensity of the two forces is approximately 480 N and 240 N (measured by a metallic sensor), with a time separation of about 0.5 ms. However, even more surprisingly than the extreme intensity and velocity of its strikes, is the ability of the mantis shrimp to hit the target up to 460 times repeatedly without significantly damaging itself (Behera and Le Ferrand, 2021). Only the

dactyl club, which is the impacting region of the appendage, suffers damage but its tissues are replaced during moulting.

Explaining how these biological structures can absorb or dissipate impact energy to minimise damage is a challenge for scientists (Meyers et al., 2006; Aizenberg et al., 2005; Wang and Gupta, 2011; Ji and Gao, 2004). In the literature, two different approaches have been used to explore the fracture toughness mechanisms of the mantis shrimp's cuticle. The first (Weaver et al., 2012; Amini et al., 2014, 2015; Raabe et al., 2005, 2006) is based on understanding the contribution of material properties to structural toughness, while the second (Claverie et al., 2011; Patek et al., 2004; Patek and Caldwell, 2005) focuses on comprehending the kinetics and dynamics of energy transfer. Regarding the first approach, the study in (Weaver et al., 2012), where the high damage tolerance of the dactyl club is explored, suggests that its particular helicoidal architecture in conjunction with the material properties are keys to the success of this biological hammer. Other researchers (Amini et al., 2015) investigated the impact surface regions of the crustacean's dactyl club and their results indicate that both the outer and the inner parts of the club include mechanisms to absorb impact energy and prevent macroscopic failure, such as interfacial sliding and rotation of fluorapatite nanorods. In addition, Grunenfelder et al. (Taylor et al., 2019) tested a set of carbon fiber-epoxy composite panels inspired by the helicoidal structure of the mantis shrimp's dactyl club and their experimental and numerical tests confirm that the helicoidal design is fundamental to enhance the residual strength and the capability to absorb damage energy and prevent crack propagation through the thickness of samples. In terms of the second approach, i.e., the kinetics and energy transfer of the impacts, fewer studies are currently available. An interesting set of works (Chen and Wang, 2014, 2015a, 2015b), for example, investigate the elastic wave propagation under dynamic loading conditions in biphasic, mineral platelets embedded in a soft matrix, and periodic bioinspired composites. As a result, it emerges that wave attenuation, functioning as a 'shielding strategy' to increase fracture toughness, is influenced by three factors: periodicity of the geometrical arrangement, hierarchical configuration of the system and excitation frequencies. Surprisingly, as far as we know, there have been no studies focused on whether the mantis shrimp uses an effective strategy to maximise the damage on the prey. Damage, in particular, is a physical process of deterioration when materials are subjected to loading. It consists, at the microscale level, in the accumulation of microstresses nearby defects or interfaces and in the related breaking or permanent deformations of the material, including the growth and coalescence of microcracks into one crack (mesoscale level), and in the propagation, stable or unstable, of the crack (macroscale level) (Lemaitre, 2012). Although with different physical structures, all materials, such as metals, alloys, polymers, composites, ceramics, rocks, concrete and wood, show similar qualitative mechanical behaviour on the meso- and macro-scales: an initial phase of elastic response, followed by yielding, with an accumulation of plastic strain, anisotropy, induced by strain, cyclic hysteresis, damage, induced by monotonic loading or by fatigue, and crack growth under static or dynamic loads (Lemaitre and Desmorat, 2005).

Understanding the mechanism of damage accumulation and material removal, even in the simplest scenario of spherical particles impacting a flat surface at normal incidence, is a difficult task (Woytowitz and Richman, 1999). In the context of metallic targets, for example, a significant amount of literature is available for the case of a single metallic projectile impacting against a metallic surface with different geometrical configurations and material properties (Gupta et al., 2001, 2007; Khan et al., 2003). Conversely, very few investigations concern the effects of multiple bullet-impacts on metallic plates. In (Hong et al., 2008), which goes in this direction, the effect of multiple shots on metallic targets having a thickness much larger than the bullet size is performed by parametrizing the separation distance between impacting points, velocities of successive hits and separation time between two consecutive impacts. It emerges that these parameters affect the residual stress

distribution in the target and, in particular, that the depth of the region where residual stresses develop increases by increasing the number of hits and impact velocities. No difference between the residual stress distributions caused by two sets of distinct double shots occurring at a separation distance equal to the diameter of the spherical bullet is found. However, as soon as this distance reduces, the analysis reveals a larger magnitude of the maximum residual stress. Regarding the effect of different time delays between two consecutive impacts, (2, 5, 10, 20) μs, no particular difference between the residual stress profiles emerges. 3D finite element simulations of impacts between rigid spherical bullets and metallic plates are presented in (Meguid et al., 1999) to investigate the shoot-peening process and the influence of shot velocity, bullet shape and separation distance between two simultaneous hits. According to the authors, a decrease in the aspect ratio of the ellipsoidal bullet leads to an increase in the depth of the target where residual stresses arise. In addition, it is reported that the dynamic of simultaneous indentations happening at different locations of the target are similar to those obtained from single shots. The shot peening process involving simultaneous and numerous impacts is also numerically analysed in (Frija et al., 2006) by measuring the superficial damage on the metallic target. Based on the Coulomb friction model, the study shows that the damage of the target increases as the friction coefficient that models the interaction between spherical bullets and flat targets increases.

Inspired by the double impact phenomenon observed during mantis shrimp predation and by considering that literature is lacking on this aspect, this paper presents finite element simulations of single and multiple (double and triple) impacts between rigid-body projectiles and flat elastic-plastic targets to quantify the damage energy dissipated by the target and to reveal which are the most damaging sequences of consecutive impacts and their optimal time delay. The material adopted for the target is metal, in order to achieve a similarity with the experimental measurements of Patek and co-workers (Patek and Caldwell, 2005) that we use as a reference to compare our results. Also, due to the high complexity of the phenomenon (Brennen, 2013), cavitation is neglected and all the strikes are assumed to be mechanical, i.e., caused by the physical interaction of the solid impactor and the target. The obtained results, reported here for the first time, can be valuable, for example, in designing safer protective armours.

2. Numerical modelling

The energy dissipated during the process of damage can be quantified by performing finite element impact simulations. Commercial finite element software, such as Abaqus (HibbettKarlsson, 1998), allows to compute the damage energy dissipated during collisions between objects. The computation is based on the 'erosion method', which requires a set of input parameters to define when the damage starts occurring and how the damage curve evolves. According to this approach, a finite element is removed from the system when its stiffness reduces to the point that its load-carrying capability becomes null. It is clear that a complete characterization of the stress-strain curve of the material is necessary to implement this method (Labonte et al., 2017). However, our aim is to investigate the damage mechanisms of multiple-hit impacts rather than focusing on a specific material. Accordingly, in the reported impact simulations, a flat elastic-plastic target is considered and, as a practical example, the mechanical properties of aluminium are used.

2.1. Geometrical and mechanical properties

As illustrated in Fig. 2, our numerical simulations involve a rigid spherical projectile and a flat target clamped on its lateral sides. Both of them are made of an elasto-plastic material that we assume to be aluminium alloy A2024-T351. Its hardening and the damage process is described by the Johnson-Cook model (Johnson and Cook, 1983), according to which the plastic flow stress takes the form

$$\overline{\sigma} = \left(A + B \bullet \overline{\varepsilon}_{pl}{}^n \right) \bullet \left[1 + C \bullet \ln \frac{\dot{\overline{\varepsilon}}_{pl}}{\dot{\varepsilon}_0} \right] \bullet \left[1 - \widehat{\theta}^m \right] \tag{1}$$

with $\overline{\sigma}$ the von Mises stress, A, B, n, m and C material parameters that need to be calibrated from experiment, $\overline{\varepsilon}_{pl}$ the equivalent plastic strain, $\dot{\overline{\varepsilon}}_{pl}$ the equivalent plastic strain rate and $\dot{\varepsilon}_0$ the reference strain rate assumed to be of unitary value (Johnson and Cook, 1983).

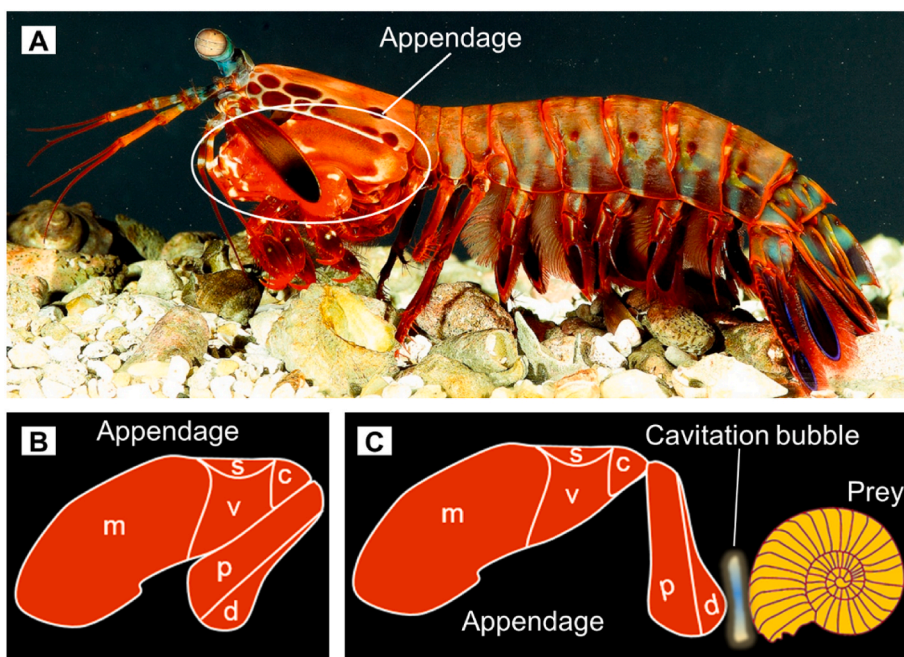Also, in Equation (1), $\widehat{\theta}$ denotes the non-dimensional temperature, given by

Fig. 1. The attack of the Odontodactylus scyllarus, commonly known as mantis shrimp. A) A resting Odontodactylus scyllarus. The white ellipse highlights the appendage that the animal uses for hunting. B) Lateral view of the raptorial appendage in a resting position showing the morphology and nomenclature of the elements: d, dactyl; p, propodus; m, merus; s, saddle; c, carpus; v, meral-V. C) Lateral view of the appendage impacting the prey. As a result of the attack a cavitation bubble arises between the retreating dactyl (marked as d in Fig. 1B) and the surface of prey.
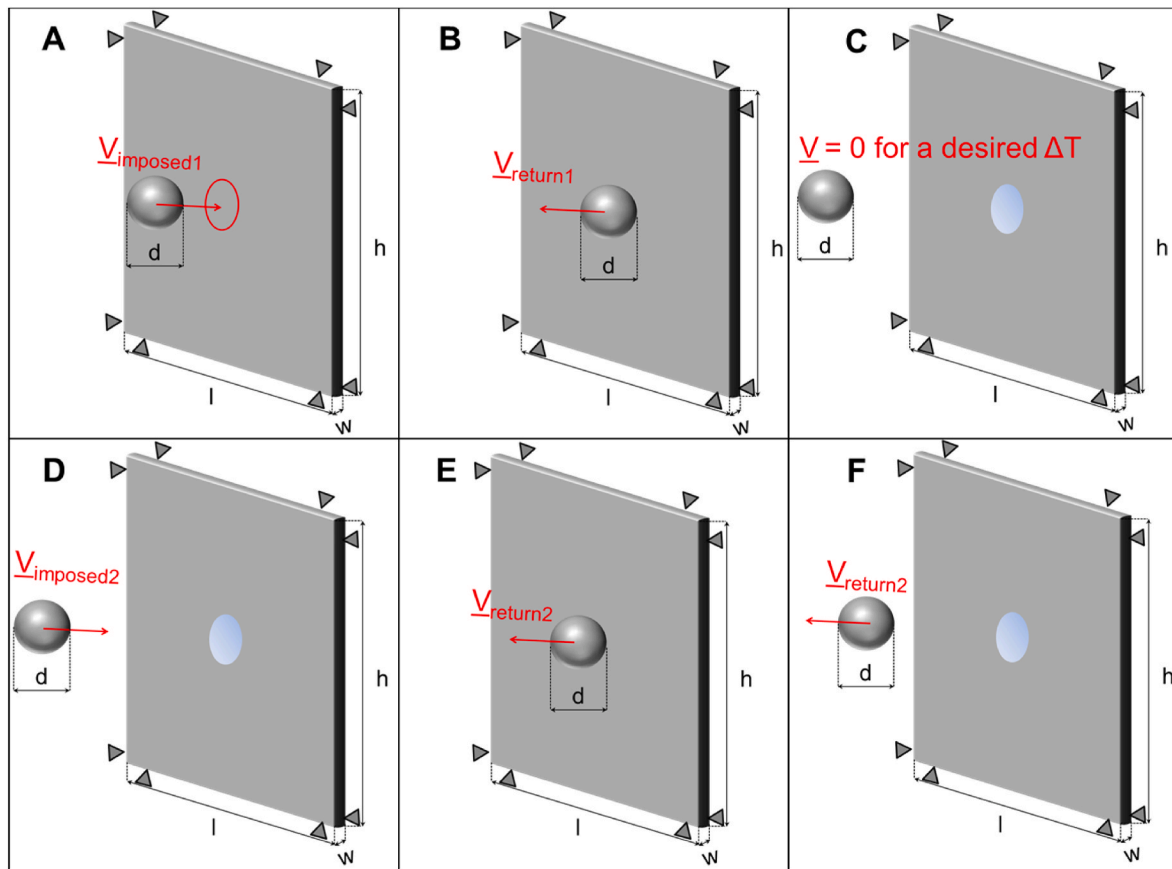
Fig. 2. Model for multiple impacts analysis made of a spherical bullet and a flat target: The figure is representative of two impact analyses where: A) the bullet travels with a first initial velocity $V_{imposed1}$, reaches the target and B) bounces back with a velocity $V_{return1}$. C) The bullet is then stopped for a desired interval of time and D) travels back toward the target with a second initial velocity $V_{imposed2}$. Once the bullet hits the target for the second time, E) it bounces back with a velocity $V_{return2}$. F) The simulation is finally stopped. The initial velocities are imposed to keep the total impact energy constant and desired energy distributions.

$$\widehat{\theta} = \begin{cases} 0 & \text{for } \theta < \theta_{trans} \\ \left(\dfrac{\theta - \theta_{trans}}{\theta_{melt} - \theta_{trans}}\right) & \text{for } \theta_{trans} \leq \theta \leq \theta_{melt} \\ 1 & \text{for } \theta > \theta_{melt} \end{cases} \quad (2)$$

being θ the current temperature, θ_{melt} the melting temperature and θ_{trans} the transition temperature, defined as the one at or below which the flow stress stops depending on the temperature.

The Johnson-Cook parameters considered in the present paper are listed in Table 1, together with the A2024-T351 material properties, i.e., elastic modulus, Poisson's ratio, density, melting and transition temperatures. The reported values, in particular, coincide with those in (Mabrouki et al., 2008).

In terms of geometry, the dimensions of the target are $l = h = 24.12$ mm and $w = 0.5$ mm (Fig. 2), values that coincide with the size of the flat sensor used for previous experiments (Patek and Caldwell, 2005).

Three different projectile's diameters are investigated, 3 mm, 4 mm and 6 mm, in order to reproduce the size of the dactyl of an adult mantis shrimp that, according to (Amini et al., 2015), is approximately 4 mm. By choosing 6 mm for the investigation of the third diameter we intended to also cover the cases where bigger dactyl sizes have been

considered for impact tests. Indeed, the smallest diameter used in (Taylor et al., 2019) for impact tests inspired by the mantis shrimp was 6 mm. Note that, for a specific size of the projectile, a constant value of mass is assumed. Finally, in the simulations the impact is modelled as a projectile that moves at an initial constant velocity, $V_{imposed1}$, hits the target for the first time, bounces back with a velocity $V_{return1}$ and immediately is halted, i.e., zero velocity, for a desired time ΔT, representing the time delay between consecutive impacts (ΔT includes the time that the projectile takes to bounce back and to travel back). Then, once the bullet has stopped for the necessary time, the simulation can either terminate, in the case of a single impact, or continue, in the case of multiple impacts. In the latter scenario, a second impact velocity, $V_{imposed2}$, is assigned to the projectile that, as previously described, hits the target and bounces back with a velocity $V_{return2}$. At this point, the simulation is stopped or, to simulate a third impact, a third impact velocity, $V_{imposed3}$, is assigned to the projectile after a time delay ΔT and the aforementioned steps are repeated. For sake of clarity, it should be noted that for all the considered configurations, illustrated in Table 2, the total impact energy is keep fixed.

Table 1
Johnson-Cook parameters and material properties used to simulate the aluminium alloy A2024-T351.

A [GPa]	B [GPa]	n	m	C	Density [Kg/m³]	Elastic Modulus [GPa]	Poisson's ratio	θ_{melt} [°C]	θ_{trans} [°C]
0.352	0.440	0.42	1	0.0083	2700	74.5	0.33	520	25

Table 2
Input velocities for single and multiple impacts with a fixed total kinetic energy $\mathscr{E} = 2.27$ J.

1 IMPACT

Bullet size [mm]	3	4	6
Velocity [m/s] ($\mathscr{E} = 2.27$ J)	345	225	122

2 IMPACTS

Bullet size [mm]	3		4		6	
= = [m/s] (0.5 $\mathscr{E}$)	244	244	159	159	86	86
1st ↑ (0.67 $\mathscr{E}$) 2nd ↓ (0.33 $\mathscr{E}$) [m/s]	282	200	184	130	100	70
1st ↓ (0.33 $\mathscr{E}$) 2nd ↑ (0.67 $\mathscr{E}$) [m/s]	200	282	130	184	70	100

3 IMPACTS

Bullet size [mm]	3			4			6		
= = = [m/s] (0.33 $\mathscr{E}$) (0.33 $\mathscr{E}$) (0.33 $\mathscr{E}$)	199	199	199	130	130	130	70	70	70
1st ↓ (0.2 $\mathscr{E}$) 2nd ↑ (0.4 $\mathscr{E}$) 3rd ↑ (0.4 $\mathscr{E}$) [m/s]	154	218	218	101	142	142	55	77	77
1st ↑ (0.5 $\mathscr{E}$) 2nd ↓ (0.25 $\mathscr{E}$) 3rd ↓ (0.25 $\mathscr{E}$) [m/s]	244	172	172	159	113	113	86	61	61
1st ↑ (0.4 $\mathscr{E}$) 2nd ↓ (0.2 $\mathscr{E}$) 3rd ↑ (0.4 $\mathscr{E}$) [m/s]	218	154	218	142	101	142	77	55	77
1st ↓ (0.25 $\mathscr{E}$) 2nd ↑ (0.5 $\mathscr{E}$) 3rd ↓ (0.25 $\mathscr{E}$) [m/s]	172	244	172	113	159	113	61	86	61
1st ↑ (0.4 $\mathscr{E}$) 2nd ↑ (0.4 $\mathscr{E}$) 3rd ↓ (0.2 $\mathscr{E}$) [m/s]	218	218	154	142	142	101	77	77	55
1st ↓ (0.25 $\mathscr{E}$) 2nd ↓ (0.25 $\mathscr{E}$) 3rd ↑ (0.5 $\mathscr{E}$) [m/s]	172	172	244	113	113	159	61	61	86

2.2. Material and failure model

Similarly to Section 2.1, the damage properties of the target are defined by the Johnson-Cook model, providing the equivalent plastic strain at the onset of damage:

$$\overline{\varepsilon_D}^{pl} = \left[d_1 + d_2 \bullet e^{(-d_3 \bullet \eta)} \right] \bullet \left[1 + d_4 \bullet ln\left(\frac{\dot{\overline{\varepsilon}}_{pl}}{\dot{\varepsilon}_0} \right) \right] \bullet \left[1 + d_5 \bullet \theta \right] \tag{3}$$

being d_1, d_2, d_3, d_4, d_5, the material-dependent failure parameters listed in Table 3 (Mabrouki et al., 2008), $\eta := -p/q$ the stress triaxiality, with p the pressure stress and q the von Mises equivalent stress.

As it can be seen in Table 3, for simplicity we have assumed $d_5 = 0$ so that no temperature effects are involved on the onset of damage.

It should be noted that Equation (3) differs from the original formula (Johnson and Cook, 1985) in the sign of the parameter d_3 since the majority of materials experiences a decrease in $\overline{\varepsilon}_D^{pl}$ with increasing the

Table 3
Damage parameters describing the onset of the damage for the aluminium A2024-T351 (Mabrouki et al., 2008).

d_1	d_2	d_3	d_4	d_5
0.13	0.13	1.5	0.011	0

stress triaxiality (HibbettKarlsson, 1998), being ductility at failure and triaxiality nonlinearly inversely proportional (Hancock and Mackenzie, 1976; Bonora, 1997).

The damage process initiates when the following criterion is satisfied

$$\omega_D = \int \frac{d\overline{\varepsilon}^{pl}}{\overline{\varepsilon_D}^{pl}} = 1 \tag{4}$$

with ω_D the state variable that increases monotonically with plastic deformation.

A stress-strain curve in the presence of damage is represented in Fig. 3.

As it can be seen, the first linear path a-b, characterising the initial elastic response of the material and terminating at the plastic yielding point, b, is followed by the strain hardening curve b-c. At point c, when $\omega_D = 1$, the damage initiates and a state of stiffness degradation begins, until the material is fully damaged, situation that happens at point e. In particular, denoted with E the Young's modulus of the material, the damage phenomenon leads to a reduction of the material stiffness to the value of $(1 - D)E$, with D the dimensionless damage variable, ranging from 0 to 1, that decreases the material load-carrying capacity.

In our simulations, for simplicity, a linear softening behavior is considered, assumption that coincides with a linear trend of the evolution curve from the onset of damage, point c, to failure, point e. The latter, in particular, is defined in terms of maximum element displacement, calculated by multiplying the value of the percent elongation at failure for the A2024-T351 aluminium alloy, $\varepsilon_e = 12\%$, by the characteristic dimension of the single finite element (diagonal). The obtained value is 0.045 mm. Also, at any given time during the analysis, the stress condition in the material is described by

$$\sigma = (1 - D)\overline{\sigma}, \tag{5}$$

where $\overline{\sigma}$ is the effective or undamaged von Mises stress, namely, the stress that would exist in absence of damage and that would follow the undamaged curve d' (Fig. 3).

When $D = 1$, a finite element loses all its load-bearing capacity and is removed from the model. Its contribution to the mass of the structure is
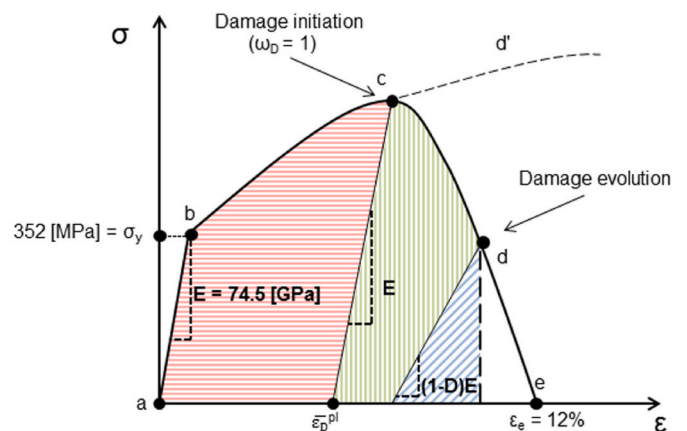
Fig. 3. Example of stress-strain response in the presence of damage. A first linear pattern (curve a-b) is followed by yielding (point b) and by the strain hardening curve (b–c). When damage initiates (point c), the stress-strain curve starts showing strain softening. During damage evolution, loading/unloading curves follow the slope $(1 - D)E$, where D is the damageable variable and E the material's Young's modulus. The material completely fails at point e. For a generic finite element at the evolution point d, the area highlighted by red horizontal lines represents the plastic strain energy per unit of volume, the area highlighted by green vertical lines is the damage dissipated energy per unit of volume and the area highlighted by blue oblique lines is the elastic strain energy per unit of volume. (For interpretation of the references to colour in this figure legend, the reader is referred to the Web version of this article.)

also eliminated.

2.3. Analysed configurations

The short time-duration force pulse that, in the biological system, is caused by cavitation here is considered as a second mechanical impact. This simplification is due to the fact that simulating the damage that cavitation bubbles cause upon collapsing is a very challenging modelling problem because of the unsteadiness of the phenomenon and of the interaction between fluid and material (Brennen, 2013). Investigating this aspect goes well beyond the scope of our simulations. Furthermore, it is important to note that although the damage is related to the energetic absorptive properties of the material, cavitation is independent of the material characteristics.

An overview of the analysed configurations and the corresponding symbols used to indicate the sequence of hits are listed in Table 4 while, in Table 2, all the settings with the associated velocities are reported.

The minimum damage energy value, in the case of one impact and 4 mm spherical projectile (corresponding to a sphere velocity of 225 m/s) for which we observed a condition of partial damage, is 2.27 J. In this configuration, the bullet provokes an hole and bounces back, as illustrated in Fig. 5b. This situation is considered as a 'limit condition' between visible damage, i.e., high damage with complete perforation of the target as in Fig. 5a, and not visible damage, i.e., minimum damage with no perforation as in Fig. 5c, and it is used to establish a comparison with the other simulations performed. Thus, in all the considered configurations, the total kinetic energy of the projectile is keep fixed and equal to 2.27 J. To calculate the velocity of the projectile for the strong and weak impact, we assume that, in the first case, the kinetic energy of the sphere doubles the one of the weak impact and, also, that the total kinetic energy related to the impacts is conserved and coinciding with the reference value $\mathscr{E} = 2.27$ J. These conditions lead to the following system of equations

$$\frac{1}{2} \bullet m_s \bullet V_{strong}^2 = 2 \bullet \frac{1}{2} \bullet m_s \bullet V_{weak}^2 \tag{6}$$

$$\frac{1}{2} \bullet m_s \bullet \sum_{i}^{2,3} V_i^2 = \mathscr{E} \tag{7}$$

with m_s the mass of the projectile, V_{strong} and V_{weak}, respectively, the projectile's velocity for the strong and weak impacts.

Different values of time delay between consecutive impacts, the parameter ΔT, are investigated: 0.0 (the value tends to 0.0), 0.2, 0.4, 0.5, 0.6, 0.8 ms. The aim is to reproduce not only the mantis shrimp attack timing that, according to the experiments in (Patek and Caldwell, 2005), is 0.5 ms, but also to explore different time delays having the same order of magnitude as the experimental data.

Finally, our explicit dynamic simulations are developed in Abaqus 6.13–3, a commercial finite element software allowing us to compute the damage energy dissipated during collisions between objects (Hibbett Karlsson, 1998). The target and the projectile are meshed by using,

Table 4
Analysed configurations and list of symbols associated with them.

Number of impacts	Symbols	Configuration
Single	–	1 single
Double	= =	2 equal
	↑↓	1st strong 2nd weak
	↓↑	1st weak 2nd strong
Triple	= = =	3 equal
	↓↑↑	1st weak 2nd strong 3rd strong
	↑↓↓	1st strong 2nd weak 3rd weak
	↑↓↑	1st strong 2nd weak 3rd strong
	↓↑↓	1st weak 2nd strong 3rd weak
	↑↑↓	1st strong 2nd strong 3rd weak
	↓↓↑	1st weak 2nd weak 3rd strong

respectively, 43,200C3D8R (8-node linear bricks, reduced integration, hourglass control) elements and 2200C3D8R elements, values obtained after a mesh convergence test (Fig. 4). Fig. 4, in particular, shows the results from the mesh convergence test used to define the sufficient number of finite elements in the central region of the target, which is the region mainly affected by the damage process.

As it can be seen, the size of the elements of the target radially increases (smaller at the centre of the target) in order to achieve an higher computational precision on the region where impacts occur. In addition, no friction coefficient is imposed to characterize the impacts but only normal behaviour ('hard' contact).

2.4. Hertzian model for dynamic impacts

The Hertzian model is implemented to explain how the penetration power of projectiles depends on their size. Specifically, by using the Hertz's theory for elastic collision (Davies, 1949), it is possible to treat the dynamics of impacts as a distributed applied static load, as explained by Davies (1949) for the case of a sphere of radius R impacting a flat target of the same material. In accordance with (Davies, 1949), at the situation of maximum compression, a circular contact surface, known as the circle of contact, arises between the two bodies. Its radius, denoted with a_m, is given by (Davies, 1949)

$$a_m = \left[2.5 \bullet \pi \bullet \rho \bullet \left(\frac{1 - \nu^2}{E} \right) \right]^{\frac{1}{5}} \bullet R \bullet V^{\frac{2}{5}} \tag{8}$$

with V the velocity of sphere, ρ, E and ν, respectively, the density, Young's modulus and Poisson's ratio of the material of both the sphere and the target. Also, the maximum value, P_m, of the total force developed during impact takes the form (Davies, 1949)

$$P_m = \frac{2}{3} \bullet (2.5 \bullet \pi \bullet \rho)^{\frac{3}{5}} \bullet \left(\frac{E}{1 - \nu^2} \right)^{\frac{2}{5}} \bullet R^2 \bullet V^{\frac{3}{2}} \tag{9}$$

relation from which the mean normal pressure at maximum compression (Davies, 1949) is

$$\overline{p}_m = \frac{P_m}{\pi \bullet a_m^2} = \frac{2}{3 \bullet \pi} \bullet (2.5 \bullet \pi \bullet \rho)^{\frac{1}{5}} \bullet \left(\frac{E}{1 - \nu^2} \right)^{\frac{4}{5}} \bullet V^{\frac{2}{5}} \tag{10}$$

and the pressure at the centre of the circle of contact, again in the condition of maximum compression (Davies, 1949),

$$p_m' = 1.5 \bullet \overline{p}_m = \frac{(2.5 \bullet \pi \bullet \rho)^{\frac{1}{5}}}{\pi} \bullet \left(\frac{E}{1 - \nu^2} \right)^{\frac{4}{5}} \bullet V^{\frac{2}{5}} \tag{11}$$

can be evaluated.

Finally, the distribution of normal pressure over the area of contact follows the law (Davies, 1949)

$$p = p_m' \bullet \frac{\sqrt{(a_m^2 - r^2)}}{a_m} \tag{12}$$

being r the distance from the centre of the circle of contact. As it can be seen, the normal pressure at a certain distance r is a function of size, velocity and material characteristics of the impacting sphere via the parameters a_m and p_m'.

3. Results and discussion

3.1. Influence of the projectile's diameter on the level of damage experienced by the target

We refer exclusively to the damage dissipated energy for our analyses and comparisons since the amount of plastic dissipated energy will be maximum at the onset of damage without changing during the
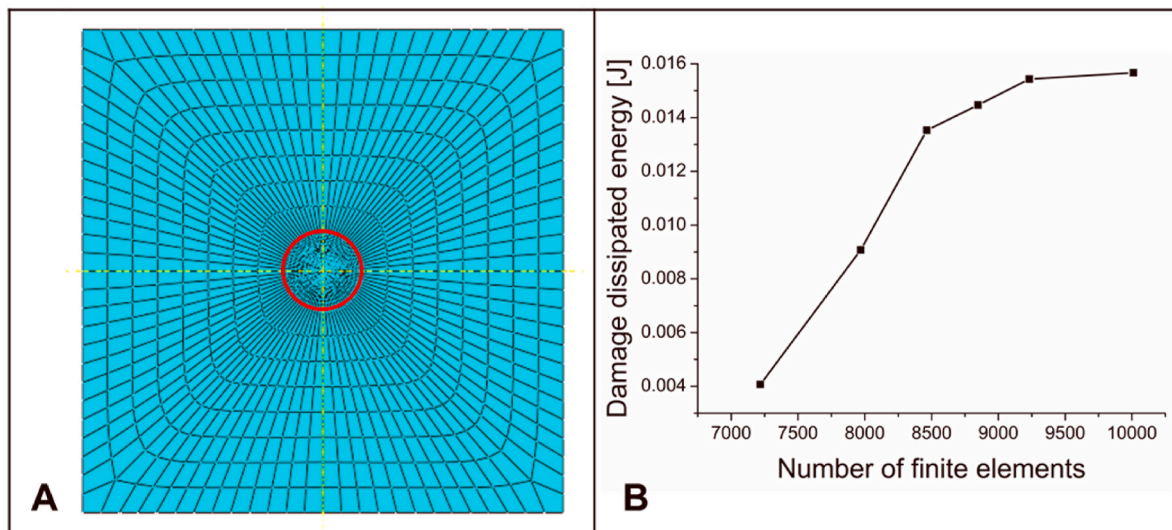
Fig. 4. Mesh convergence test for the central region of the target. A) The mesh is obtained after partitioning the geometry into many sub-regions. B) Mesh convergence test for the case 'single-impact, 4 mm bullet', performed to define the sufficient number of finite elements in the central circular region (highlighted in red in Fig. 4A) having the same diameter of the bullet. (For interpretation of the references to colour in this figure legend, the reader is referred to the Web version of this article.)

damage evolution of a specific finite element (Fig. 3).

The results of our simulations are illustrated in Figs. 5–9. Generally, depending on the size of the projectile, three different types of damage are experienced by the target: high damage, with the projectile that hits and perforates the target, partial damage, with the formation of a central hole but without penetration, and minimum damage, with the projectile that hits the target and bounces back without notable structural damage. All the values of energy are computed from postprocessing and are associated with the final state of the plate (after the sequence of impacts). The described scenarios are experienced, on order, for the cases of 3 mm, 4 mm and 6 mm diameter of the impacting solid (Fig. 5). This expected result agrees with the Hertz's theory presented in Section 2.4 and it is also confirmed from Figs. 6–8 where, as shown, the highest value of damage dissipated energy corresponds to the 3 mm diameter. Conversely, for the 6 mm diameter, the smallest amount of damage energy dissipated by the target is observed. It can be thus said that the smaller the sphere, the higher will be the penetration power.

A second consideration can be made by focusing on Fig. 8, where a sensitive analysis for the three diameters of the projectile is reported. By considering all the 11 configurations for single and multiple impacts and averaging the corresponding damage energies, it emerges that the 4 mm diameter has the highest standard deviation so that, for this impactor size, it can be concluded that results are very sensitive and strongly dependent on the different configurations. This particular behavior is also observed in Figs. 6 and 7 where, differently from the other two diameters considered, the 4 mm projectile displays highly oscillatory curves with a number of peaks corresponding to certain impact configurations.

3.2. Maximization of damage under particular impact configurations

Figs. 6 and 7 also reveals that the level of damage on the target is strongly affected by the interval ΔT between consecutive impacts and by the impact protocol, namely, by the different combinations of equal, =, weak, ↓, or strong, ↑, impacts (cf. Tables 2 and 4). Specifically, it emerges what follows.

a. 6 mm projectile (minimum damage): this diameter provides the lowest values of damage dissipated energy, independently of the impact combination and interval ΔT. As reported in Figs. 6 and 7, no peaks or particular trends emerge, being the values of damage

dissipated energy for single and multiple impacts included in the range 0.48–1.53 mJ. Specifically, the highest value corresponds to the one-impact configuration, while a reduction of approximately 20% and 60% is experienced in the case of two- and three-impacts configuration, on order.

b. 4 mm projectile (partial damage): overall, results reveal that, in terms of damage, it is more effective to concentrate all the kinetic energy in one impact, being the amount of damage energy dissipated by the target of 15.78 mJ, the highest among the considered configurations (Figs. 6 and 7). Conversely, splitting the kinetic energy in two impacts reduces the damage of the target by more than 70% (Fig. 6) while a reduction of approximately 80% is observed in the case of three impacts (Fig. 7). Also, for this particular value of the projectile's diameter, an oscillatory pattern with multiple maxima in the damage energy can be seen in Figs. 6 and 7. This trend is more evident in the case of a double impact and, in particular, for the configuration ↑↓, i.e., first impact strong and second impact weak, for which three peaks located at ΔT =(0.3, 0.5, 0.8) ms are observed. However, by focusing on the double-impact configurations in Fig. 6, it emerges that the highest level of damage is provided by the configuration ↑↓ with a time delay of 0.5 ms, namely, by the configuration that reproduces the dynamics that the mantis shrimp adopts: a first strong impact followed, after a delay of 0.5 ms, by a second impact twice weaker than the first. This result is confirmed in Fig. 9, where the three different combinations of double impacts ↑↓, ↓↑, and = = are investigated by assuming a time delay between consecutive impacts of ΔT = 0.5 ms. As illustrated, after the second impact, the highest level of damage corresponds to the configuration ↑↓ with a portion of the target detached while, for the configurations ↓↑ and = =, no visible damage is provided, being the projectile bounced back without visibly damaging the target. Regarding the three-impacts configuration in Fig. 7, a more complex scenario emerges, with the configuration ↑↓↑ leading to the highest level of damage: 9.7 mJ for a time delay ΔT = 0.5 ms.

c. 3 mm projectile (high damage): as stated in Section 3.1, notwithstanding the impact configuration considered, i.e., single, double or triple impact, the 3 mm projectile displays the highest level of damage energy. However, even if the highest peak of damage energy dissipated, 24.04 mJ, is recorded for the configuration ↓↓↑↑ with a time delay ΔT = 0.0 ms, it can be said that, differently from the previous two cases, a qualitatively similar outcome emerges for the
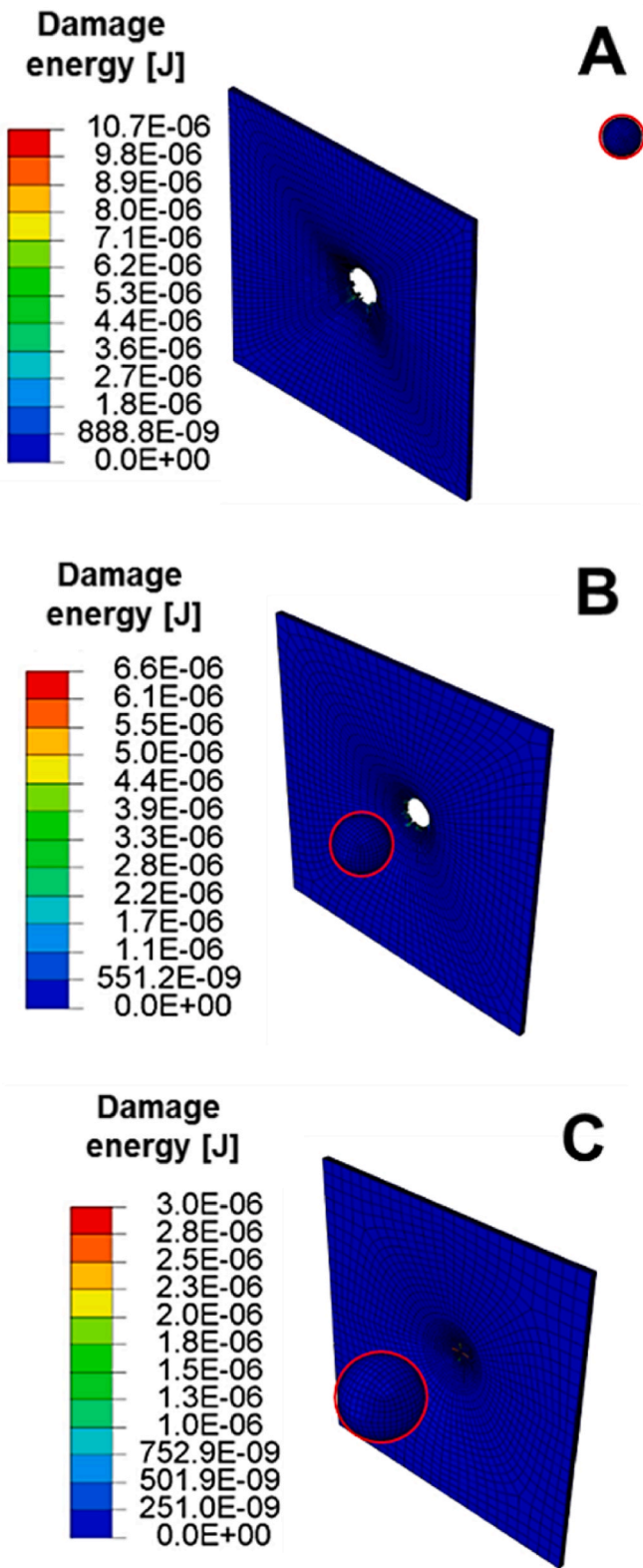
Fig. 5. Three different types of damage for the three sizes of the projectile. A) High damage: complete perforation with a 3 mm diameter bullet. B) Partial damage: the 4 mm diameter bullet bounces back after provoking a hole on the target. C) Minimum damage: non-penetrating damage with a 6 mm diameter bullet. Images are taken in the last instant of the simulations involving a generic double impact.
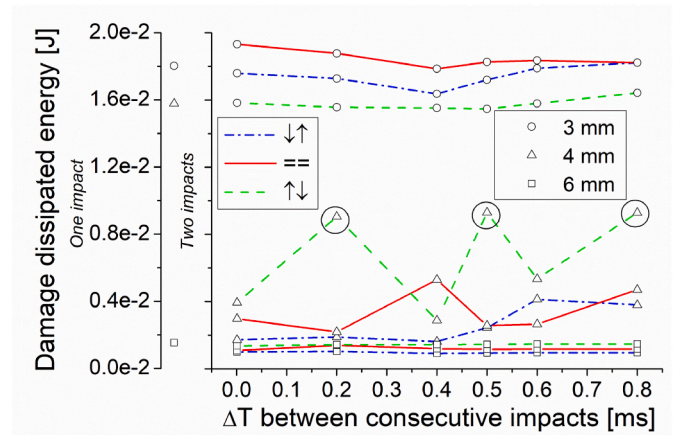

Fig. 6. One/two impact configurations (kinetic energy 2.27 J). It is observed that for the intermediate impactor size, there are maxima for damage at three separate values of ΔT = (0.2, 0.5, 0.8) ms (black circles), while a similar behaviour is not observed for the other two impactor sizes.
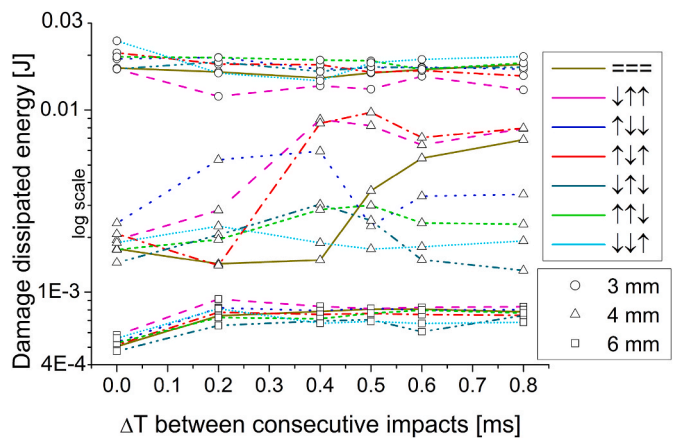

Fig. 7. Three impacts configuration (kinetic energy = 2.27 J) in a log scale graph.
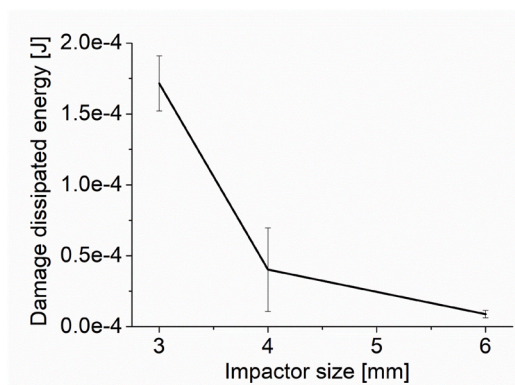

Fig. 8. 'Sensitivity analysis' for the three sizes of the bullet. The values are obtained by averaging the damage energies from all the 11 configurations for single and multiple impacts. The vertical lines represent the standard deviation of the values. The highest standard deviation is observed for the 4 mm bullet, showing the high scattering of results.

single-, double- and triple-impact configurations. As it can be seen, the measured values of damage energy are very similar, being the difference between the one-impact configuration, 18.02 mJ, and the
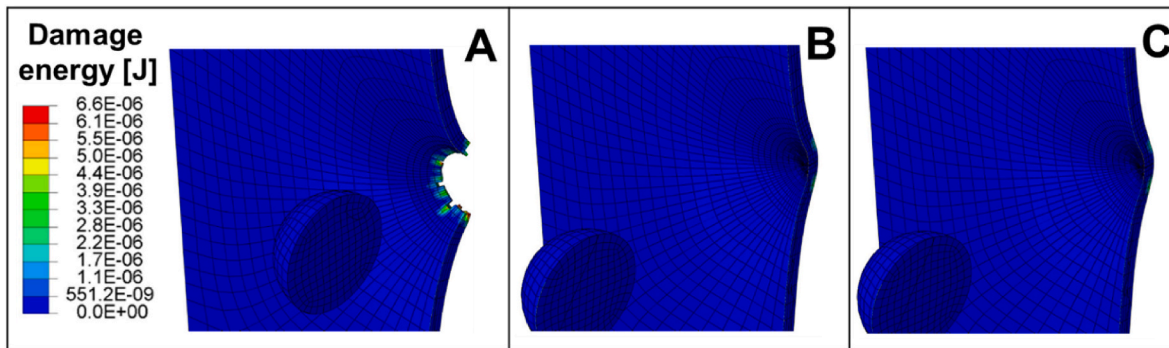
Fig. 9. Double impact for 4 mm bullet, with a ΔT of 0.5 ms. Figures show the final instant (once simulations stopped) after the second impact. A) ↑↓, B) ↓↑, C) = = . Only for the configuration A) part of the target is detached from the structure once the bullet hits it for the second time.

two-impacts and three-impacts ones of approximately 4% and 5%, respectively. Finally, the lowest level of damage energy, 11.91 mJ, is recorded for the triple-impact case ↓↑↑ having a time delay of ΔT = 0.2 ms.

4. Possible explanations to the damage maximization

As stated in Section 3, independently of the impact configuration considered, the 3 mm projectile provides the highest level of damage on the target while the lowest values are experienced by the projectile having a diameter of 6 mm. Also, among the double-impact configurations, it emerges that the ↑↓ with a time delay of ΔT = 0.5 ms, i.e., first strong impact followed, after 0.5 ms, by a second impact twice weaker than the first, is the most damaging for the 4 mm projectile. In terms of damage, this particular configuration displays an oscillatory trend with multiple peaks located at different values of ΔT. This behavior, as revealed by our analysis, is more evident for the 4 mm projectile.

The aim of this section is to find a possible explanation to the origin of these results.

4.1. Hertzian model to explain the high penetration power of the 3 mm projectile

Let us focus on Equation (12), allowing us to evaluate the distribution of the normal pressure that the projectile exerts on the target, as a function of the distance from the centre of the contact surface. By considering, for simplicity, the velocity corresponding to the single-impact configuration, 345 m/s for the 3 mm projectile, 225 m/s for the 4 mm projectile and 122 m/s for the 6 mm projectile, the pressure distribution for the three examined diameters is reported in Fig. 10.

For sake of clarity, it should be noted that the Hertzian model is linear elastic and does not include plastic deformation and damage mechanisms. However, even if the graphs do not represent the real level of pressure occurring on the contact surface, they are a useful tool to analyse the penetration power of projectiles having a certain mass and velocity.

As illustrated in Fig. 10, the smaller the diameter, the higher will be the pressure at the centre of the contact surface. Also, as the projectile becomes smaller, the contact surface, that is the area of the target affected by the contact stresses exerted by the impactor, significantly reduces. Thus, in dealing with projectiles having a small diameter, 3 mm in the present case, we obtain the situation in which high stresses are distributed over a small area, with a peak of stress located at the centre. This explains the high penetration power of the 3 mm projectile and, in general, of projectiles having a smaller and smaller diameter.
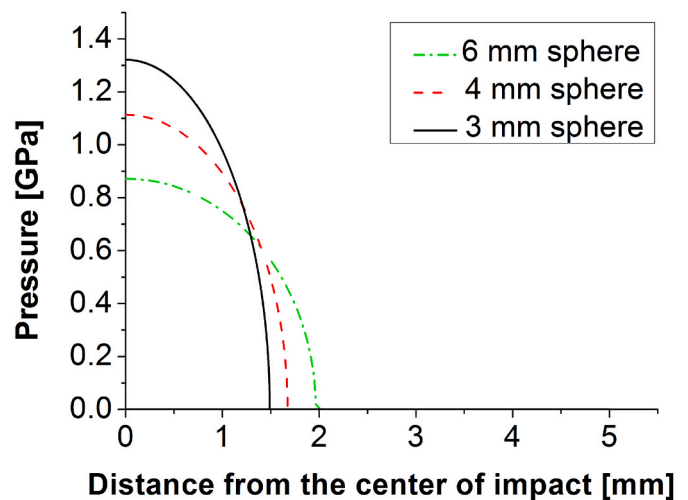

Fig. 10. Pressure distribution for the three examined diameters of the projectile. The smallest projectile size, 3 mm, results in a higher pressure at the centre of the contact surface and in a smaller area affected by contact stresses. The kinetic energy of impacts is constant and equal to 2.27 J.

4.2. Modal analysis to investigate possible resonance phenomena for the double-impact configuration with a 4 mm projectile

Modal analysis is performed to verify the existence of resonance phenomena, which amplify the response of the target and, in particular, the level of damage observed in the case of double-impact configuration with a 4 mm projectile.

Modal analysis consists in solving the eigenvalue problem

$$\left(-\omega^2\,\mathbf{M}+\mathbf{K}\right)\boldsymbol{\varphi}=0 \tag{13}$$

allowing us to find the natural mode frequencies, *ω,* and corresponding natural mode shapes, *φ,* of a structure having mass **M** and stiffness **K** (Ewins, 1984).

With reference to the examined scenario, i.e., the target subjected to double impact and projectile having a diameter of 4 mm, the outcome of the analysis is illustrated in Table 5, where a comparison between the target's natural mode frequency and the force's frequency is reported for different values of time delay ΔT. For sake of clarity, the force's frequency is calculated as the number of impacts, two for this specific case, over the considered ΔT, i.e., time delay between consecutive impacts. It emerges that one of the applied forces has a frequency similar to the fundamental frequencies of the target, so that the influence of resonance phenomena on the damage mechanism cannot be excluded.

Table 5
Comparison between the force frequency values and the first five natural mode frequency values of the target. The first value in the second column (7730 Hz) is simular to the first two values in first column.

Force frequency [Hz]	Target natural mode frequency [Hz]
10000 (for ΔT = 0.2)	7730
5000 (for ΔT = 0.4)	15912
4000 (for ΔT = 0.5)	15953
3333 (for ΔT = 0.6)	23709
2500 (for ΔT = 0.8)	28149

4.3. The oscillatory motion of the target as a possible explanation to the oscillations in the level of damage observed for the ↑↓ configuration

We hypothesize that the dynamics of oscillations, which the target exhibits after the first hit, has an important influence over the measured deformation and damage. During multiple collisions, the stiffness, boundary conditions and dimensions of the target are critical in determining its unloading process once the projectile bounces back. In particular, by considering the collision to be perfectly inelastic and assuming no variation of potential energy, the dissipated energy, $\mathscr{E}_d$, takes the form

$$\mathscr{E}_d = \Delta K = K_i - K_f = \frac{1}{2} \, m_s \bullet v_s^2 + \frac{1}{2} \, m_t \bullet v_t^2 - \frac{1}{2} \bullet (m_s + m_t) \bullet V^2 =$$
$$= \frac{1}{2} \bullet \frac{m_s \bullet m_t}{(m_s + m_t)} \bullet \left(v_s^2 + v_t^2 - 2 \bullet v_s \bullet v_t\right) \qquad (14)$$

with K_i and K_f the initial and final kinetic energy of the whole system, m_s and m_t the masses of the projectile and of the target, v_s and v_t their velocities before colliding, V the velocity of both bodies after the collision. It is important to remark that the term m_t in Equation (14) in our case is not a constant and is dynamically updated when fully damaged finite elements are removed from the system (Section 2.2).

From Equation (14) it emerges that the dissipated energy increases by increasing the relative velocity between the target and the projectile, so that the local velocity of the plate at the onset of the second, or third, collision affects significantly the amount of energy dissipated. In this sense, we hypothesize that the oscillatory motion of the plate is responsible for the different results observed by varying ΔT. To make it more clear, let us focus on Fig. 11, representing the velocity curves of a node located in the central part of the target for the ↑↓ configuration with a 4 mm projectile. Two different time delays are considered: ΔT = 0.4 ms (Fig. 11a), to which no peaks correspond, and ΔT = 0.5 ms (Fig. 11b), identifying a peak in the considered configuration.

Taking into account that, in our convention, the velocity of the projectile is negative when it moves towards the target, Fig. 11 reveals that to positive velocities of the target, i.e., opposite to the projectile, corresponds a peak in the damage energy dissipated (cf. Fig. 6) while an opposite behavior emerges for negative velocities. In other words, when the impacting body and the local oscillating portion of the target impact with opposite velocities, we observe the peaks in the damage energy curves reported in Fig. 6. In our simulations, these oscillations are induced by the imposed boundary conditions, coinciding with the four sides of the target clamped, and by the material and geometrical properties of the target. However, even if, in the real scenario, the shell of preys, such as snails, crustaceans and fishes, are less flexible and the oscillations are less evident, it is still possible to hypothesize that such oscillating non-stationary phenomena occur and may have a role in the energy dissipation mechanism.

These observations, derived for the double-impact configuration, also apply for the triple-impact case.

4.4. Further simulations to investigate if the maximum level of damage provided by ↑↓ with ΔT = 0.5 ms is material- or geometry-dependent

Having identified the ↑↓ configuration as the double-impact scenario causing the highest level of damage for the 4 mm projectile, we decided to perform additional simulations to further investigate this particular configuration. Our intention, in particular, is to verify if this result has a general extent or if it is affected by the particular geometry, material properties and inertia of the target. To go in this direction, we have examined the following situations.

1) *Different material properties.* This case involves a target having the original geometry but a different value of the yield stress, which is increased from the original 352 MPa to 752 MPa. This will allow the target to dissipate more energy via plastic deformation and less energy via damage.
2) *Smaller target.* Here the target has the original material properties but a modified geometry: from the original (24.1 × 24.1 × 0.5) mm to (12.05 × 12.05 × 0.5) mm.
3) *Larger target.* Again, the target has the original material properties but a modified geometry that varies from the original (24.1 × 24.1 × 0.5) mm to (30 × 30 × 0.5) mm.

The outcome of our analysis is presented in Fig. 12. As it can be seen, the curves corresponding to the three examined configurations display a peak for ΔT = 0.5 ms, revealing that this particular time delay, previously identified as the one providing the maximum damage (cf. Section 3.1), remains the best choice to obtain the maximum level of damage,
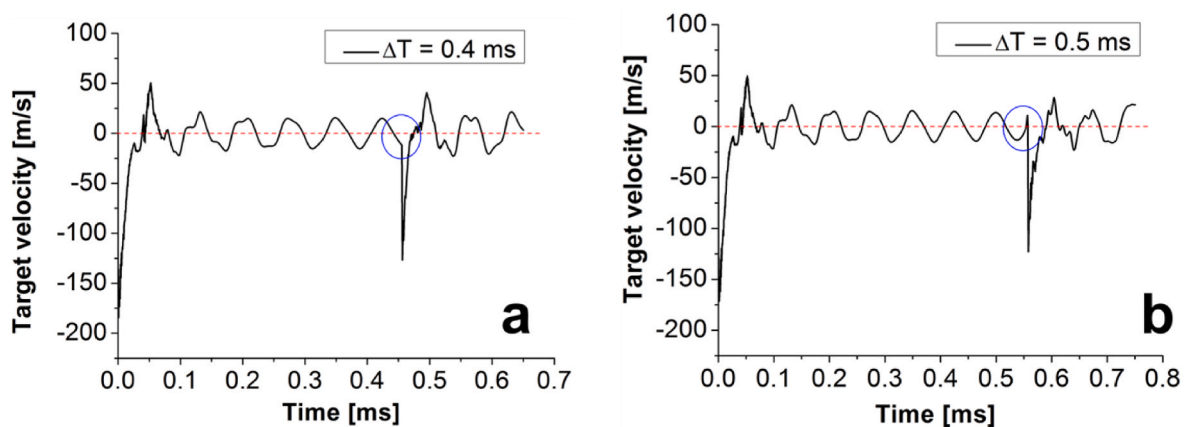
Fig. 11. Results for different material properties and sizes of the target. Curves corresponding to the double-impact configuration ↑↓ with a 4 mm projectile. Each curve experiences a peak value for the time delay ΔT = 0.5 ms (blue circles), as confirmed by the previous set of simulations (cf. *Section 3.1*) (For interpretation of the references to colour in this figure legend, the reader is referred to the Web version of this article.)
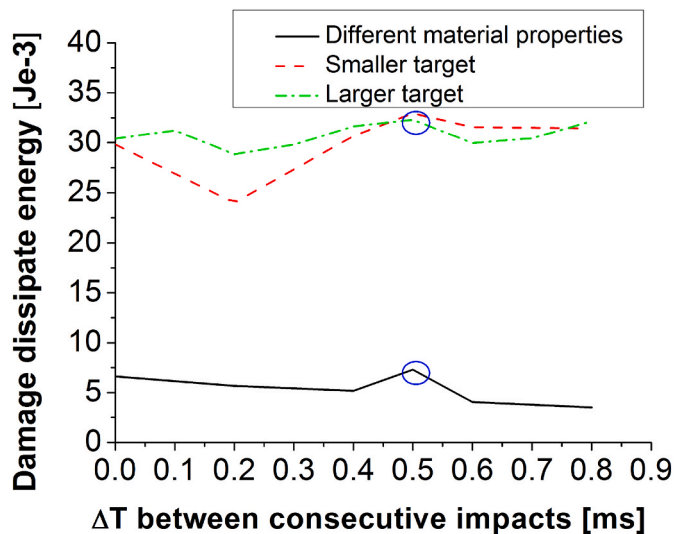
Fig. 12. Velocity curves of a single node on the central part of the target for the ↑↓ configuration: a) $\Delta T = 0.4$ ms, b) $\Delta T = 0.5$ ms.

independently of the mechanical and geometrical characteristics of the target. It can be thus said that, for the double-impact configuration ↑↓ with a 4 mm projectile, the time delay $\Delta T = 0.5$ ms is the optimal value for the maximization of damage. This scenario, in particular, coincides with the strategy adopted by the mantis shrimp to kill its preys.

5. Conclusions

This paper, inspired by the double-impact strategy adopted to predate by the *Odontodactylus scyllarus*, a crustacean known as mantis shrimp, presents a set of parametric finite element simulations aimed at investigating the damaging effects provided by multiple impacts. Elasto-plastic projectiles and target are used while, to mimic the impact parameters found in the mantis shrimp's attack, three different projectile's diameters, (3, 4, 6) mm, and six different time delays between consecutive impact, (0.0, 0.2, 0.4, 0.5, 0.6, 0.8) ms, are examined. The first approximate the size of the crustacean's appendage, the second reproduce the timings of its assaults. Finally, in all the considered configurations, the total impact energy is keep fixed at the value of 2.27 J and distributed among single-, double- or triple-impact scenarios by changing the projectile's velocity.

It emerges that the single-impact configuration is the most damaging while, among the double-impact configurations analysed, the strategy adopted by the mantis shrimp leads to the highest level of damage. To verify if the latter result is material- or geometry-dependent, a second set of finite element simulations are performed, involving a target having different mechanical properties, i.e., an higher yield stress, and modified geometric characteristics, i.e., smaller and larger domain. Also in this case, the mantis shrimp's strategy remains the optimal solution to achieve the maximum level of damage. However, further studies are necessary to extend our results. For instance, it would be useful to experimentally measure forces and timing of the crustacean attacks for targets made of different materials, to investigate if and how the animal adapts its strategy to the surface it faces. Simultaneously, to understand if the animal's strategy is the most damaging, it would be opportune to reproduce these experimental scenarios and quantify the damage by fluid-structure interaction simulations. Regarding the triple-impact configurations, more complex scenarios are obtained and different optimal solutions are found. In addition, independently of the impact configuration considered, the 3 mm projectile and the 6 mm projectile provide, on order, the highest and the lowest level of damage on the target. This result, in accordance with the Hertzian model for dynamic impacts, confirms the high penetration power of smaller projectiles.

It should be noted that the aim of this paper is not to reproduce the real predator-prey scenario but to only capture the relevant mechanics and verify the existence of optimal damaging strategies for a fixed amount of kinetic energy of the impactor and for generic material properties of the target. Indeed, only the heel of the mantis shrimp's appendage resembles a sphere, as modelled in our simulations, and the preys' outer shells, usually snails, have complicated spiral geometries. In addition, mechanical properties of both the mineralized chitin composite constituting the mantis shrimp's dactyl and the highly mineralized nacre shells are different from aluminium. However, the arbitrariness of the assumptions behind our model, coupled with our results, lead us to hypothesize that the shrimp may use an 'optimal' damaging strategy.

Declaration of competing interest

The authors declare that they have no known competing financial interests or personal relationships that could have appeared to influence the work reported in this paper.

Data availability

Data will be made available on request.

Acknowledgments

References

Aizenberg, J., Weaver, J.C., Thanawala, M.S., Sundar, V.C., Morse, D.E., Fratzl, P., 2005. Skeleton of Euplectella sp.: structural hierarchy from the nanoscale to the macroscale. Science 309 (5732), 275–278.

Amini, S., Masic, A., Bertinetti, L., Teguh, J.S., Herrin, J.S., Zhu, X., Su, H., Miserez, A., 2014. Textured fluorapatite bonded to calcium sulphate strengthen stomatopod raptorial appendages. Nat. Commun. 5.

Amini, S., Tadayon, M., Idapalapati, S., Miserez, A., 2015. The role of quasi-plasticity in the extreme contact damage tolerance of the stomatopod dactyl club. Nat. Mater. 14 (9), 943–950.

Behera, R.P., Le Ferrand, H., 2021. Impact-resistant materials inspired by the mantis shrimp's dactyl club. Matter 4, 2831–2849.

Bonora, N., 1997. On the effect of triaxial state of stress on ductility using nonlinear CDM model. Int. J. Fract. 88 (4), 359–371.

Brennen, C.E., 2013. Cavitation and Bubble Dynamics. Cambridge University Press.

Burrows, M., Hoyle, G., 1972. Neuromuscular physiology of the strike mechanism of the mantis shrimp, Hemisquilla. J. Exp. Zool. 179 (3), 379–393.

Butler, R.W., Kirbyson, J.W., 1979. Oyster predation by the black oystercatcher in British Columbia. Condor 81 (4), 433–435.

Caldwell, R.L., Dingle, H., 1975. Ecology and evolution of agonistic behavior in stomatopods. Naturwissenschaften 62 (5), 214–222.

Caldwell, R.L., Dingle, H., 1976. Stomatopods. Sci. Am. 234 (1), 80–89.

Carlin, N.F., Gladstein, D.S., 1989. The "bouncer" defense of Odontomachus ruginodis and other odontomachine ants (Hymenoptera: formicidae). Psyche 96 (1–2), 1–20.

Chen, Y., Wang, L., 2014. Tunable band gaps in bio-inspired periodic composites with nacre-like microstructure. J. Appl. Phys. 116 (6), 063506.

Chen, Y., Wang, L., 2015a. Multiband wave filtering and waveguiding in bio-inspired hierarchical composites. Extreme Mechanics Letters 5, 18–24.

Chen, Y., Wang, L., 2015b. Bio-inspired heterogeneous composites for broadband vibration mitigation. Sci. Rep. 5, srep17865.

Chen, P., Y, McKittrick, J., Meyers, M.A., 2012. Biological materials: functional adaptations and bioinspired designs. Prog. Mater. Sci. 57, 1492–1704.

Claverie, T., Chan, E., Patek, S.N., 2011. Modularity and scaling in fast movements: power amplification in mantis shrimp. Evolution 65 (2), 443–461.

Clutton-Brock, T., 1988. Reproductive Success: Studies of Individual Variation in Contrasting Breeding Systems. University of Chicago Press.

Cronin, T.W., Marshall, N.J., 1989. A retina with at least ten spectral types of photoreceptors in a mantis shrimp. Nature 339 (6220), 137–140.

Cronin, T.W., Caldwell, R.L., Marshall, J., 2001. Sensory adaptation: tunable colour vision in a mantis shrimp. Nature 411 (6837), 547–548.

Currey, J.D., Landete-Castillejos, T., Estevez, J., Ceacero, F., Olguin, A., Garcia, A., Gallego, L., 2009. The mechanical properties of red deer antler bone when used in fighting. J. Exp. Biol. 212 (24), 3985–3993.

Davies, R., 1949. In the determination of static and dynamic yield stresses using a steel ball. In: Proceedings of the Royal Society of London A: Mathematical, Physical and Engineering Sciences. The Royal Society, pp. 416–432.

Dingle, H., Caldwell, R.L., 1969. The aggressive and territorial behaviour of the mantis shrimp Gonodactylus bredini Manning (Crustacea: Stomatopoda). Behaviour 33 (1), 115–136.

Ewins, D.J., 1984. Modal Testing: Theory and Practice, vol. 15. Research studies press Letchworth.

Frija, M., Hassine, T., Fathallah, R., Bouraoui, C., Dogui, A., de Génie Mécanique, L., 2006. Finite element modelling of shot peening process: prediction of the compressive residual stresses, the plastic deformations and the surface integrity. Mater. Sci. Eng., A 426 (1), 173–180.

Gronenberg, W., 1995. The fast mandible strike in the trap-jaw ant Odontomachus. J. Comp. Physiol. 176 (3), 399–408.

Gupta, N., Ansari, R., Gupta, S., 2001. Normal impact of ogive nosed projectiles on thin plates. Int. J. Impact Eng. 25 (7), 641–660.

Gupta, N., Iqbal, M., Sekhon, G., 2007. Effect of projectile nose shape, impact velocity and target thickness on deformation behavior of aluminum plates. Int. J. Solid Struct. 44 (10), 3411–3439.

Gupta, H., Krauss, S., Kerschnitzki, M., Karunaratne, A., Dunlop, J., Barber, A., Boesecke, P., Funari, S., Fratzl, P., 2013. Intrafibrillar plasticity through mineral/collagen sliding is the dominant mechanism for the extreme toughness of antler bone. J. Mech. Behav. Biomed. Mater. 28, 366–382.

Hancock, J., Mackenzie, A., 1976. On the mechanisms of ductile failure in high-strength steels subjected to multi-axial stress-states. J. Mech. Phys. Solid. 24 (2–3), 147–160.

Hang, F., Gupta, H.S., Barber, A.H., 2014. Nanointerfacial strength between non-collagenous protein and collagen fibrils in antler bone. J. R. Soc. Interface 11 (92), 20130993.

Haslam, M., Fujii, J., Espinosa, S., Meyer, K., Ralls, K., Tinker, M., T, et al., 2019. Wild sea otter mussels pounding leaves archaeological traces. Sci. Rep. 9, 1–11.

Hibbett, Karlsson, 1998. Sorensen, *ABAQUS/standard: User's Manual*. Hibbitt, vol. 1. Karlsson & Sorensen.

Hong, T., Ooi, J., Shaw, B., 2008. A numerical simulation to relate the shot peening parameters to the induced residual stresses. Eng. Fail. Anal. 15 (8), 1097–1110.

Ji, B., Gao, H., 2004. Mechanical properties of nanostructure of biological materials. J. Mech. Phys. Solid. 52 (9), 1963–1990.

Johnson, G.R., Cook, W.H., 1983. In A constitutive model and data for metals subjected to large strains, high strain rates and high temperatures. In: Proceedings of the 7th International Symposium on Ballistics, the Hague, The Netherlands, pp. 541–547.

Johnson, G.R., Cook, W.H., 1985. Fracture characteristics of three metals subjected to various strains, strain rates, temperatures and pressures. Eng. Fract. Mech. 21 (1), 31–48.

Khan, W., Ansari, R., Gupta, N., 2003. Oblique impact of projectile on thin aluminium plates. Defence Sci. J. 53 (2), 139.

Kitchener, A., 1987. Fracture toughness of horns and a reinterpretation of the horning behaviour of bovids. J. Zool. 213 (4), 621–639.

Labonte, D., Lenz, A.-K., Oyen, M.L., 2017. On the relationship between indentation hardness and modulus, and the damage resistance of biological materials. Acta Biomater. 57, 373–383.

Lazarus, B.S., Velasco-Hogan, A., Gomez-del Rio, T., Meyers, M., A, Jasiuk, I., 2020. A review of impact resistant biological and bioinspired materials and structures. J. Mater. Res. Technol. 9 (6), 15705–15738.

Lemaitre, J., 2012. A Course on Damage Mechanics. Springer Science & Business Media.

Lemaitre, J., Desmorat, R., 2005. Engineering Damage Mechanics: Ductile, Creep, Fatigue and Brittle Failures. Springer Science & Business Media.

Mabrouki, T., Girardin, F., Asad, M., Rigal, J.-F., 2008. Numerical and experimental study of dry cutting for an aeronautic aluminium alloy (A2024-T351). Int. J. Mach. Tool Manufact. 48 (11), 1187–1197.

Meguid, S., Shagal, G., Stranart, J., Daly, J., 1999. Three-dimensional dynamic finite element analysis of shot-peening induced residual stresses. Finite Elem. Anal. Des. 31 (3), 179–191.

Meyers, M.A., Lin, A.Y., Seki, Y., Chen, P.-Y., Kad, B.K., Bodde, S., 2006. Structural biological composites: an overview. JOM (J. Occup. Med.) 58 (7), 35–41.

Meyers, M.A., Chen, P., Y, Lin, A., Y M, Seki, Y., 2008b. Biological materials: structure and properties. Prog. Mater. Sci. 53, 1–206.

Parsons, K.J., Spence, A.J., Morgan, R., Thompson, J.A., Wilson, A.M., 2011. High speed field kinematics of foot contact in elite galloping horses in training. Equine Vet. J. 43, 216–222.

Patek, S.N., 2019. The power of mantis shrimp strikes: interdisciplinary impacts of an extreme cascade of energy release. Integr. Comp. Biol. 59, 1573–1585.

Patek, S., Caldwell, R., 2005. Extreme impact and cavitation forces of a biological hammer: strike forces of the peacock mantis shrimp Odontodactylus scyllarus. J. Exp. Biol. 208 (19), 3655–3664.

Patek, S., Korff, W., Caldwell, R., 2004. Biomechanics: deadly strike mechanism of a mantis shrimp. Nature 428 (6985), 819–820.

Raabe, D., Sachs, C., Romano, P., 2005. The crustacean exoskeleton as an example of a structurally and mechanically graded biological nanocomposite material. Acta Mater. 53 (15), 4281–4292.

Raabe, D., Romano, P., Sachs, C., Fabritius, H., Al-Sawalmih, A., Yi, S.-B., Servos, G., Hartwig, H., 2006. Microstructure and crystallographic texture of the chitin–protein network in the biological composite material of the exoskeleton of the lobster Homarus americanus. Mater. Sci. Eng. 421 (1), 143–153.

Tadayon, M., Amini, S., Wang, Z., Miserez, A., 2018. Biomechanical design of the mantis shrimp saddle: a biomineralized spring used for rapid raptorial strikes. Cell Press 8, 271–282.

Taylor, J.R., Scott, N.I., Rouse, G.W., 2019. Evolution of mantis shrimp telson armour and its role in ritualized fighting. J. R. Soc. Interface 16 (157), 20190203.

Thoen, H.H., How, M.J., Chiou, T.-H., Marshall, J., 2014. A different form of color vision in mantis shrimp. Science 343 (6169), 411–413.

Wang, R., Gupta, H.S., 2011. Deformation and fracture mechanisms of bone and nacre. Annu. Rev. Mater. Res. 41, 41–73.

Wang, L.Z., Lu, S., Liu, X.Y., Niu, X.F., Wang, C., Ni, Y.K., et al., 2013. Biomechanism of impact resistance in the woodpecker's head and its application. Sci. China Life Sci. 56, 715–719.

Weaver, J.C., Milliron, G.W., Miserez, A., Evans-Lutterodt, K., Herrera, S., Gallana, I., Mershon, W.J., Swanson, B., Zavattieri, P., DiMasi, E., 2012. The stomatopod dactyl club: a formidable damage-tolerant biological hammer. Science 336 (6086), 1275–1280.

Woytowitz, P., Richman, R., 1999. Modeling of damage from multiple impacts by spherical particles. Wear 233, 120–133.